RSC Advances

PAPER

View Article Online
View Journal | View Issue

Cite this: *RSC Adv.*, 2020, **10**, 25717

Effects of high mechanical treatment and long-term annealing on crystal structure and thermal stability of Ti_2O_3 nanocrystals

Albina A. Valeeva,*[ab] Svetlana Z. Nazarova,[a] Hartmuth Schröttner,[c] Evgeny Yu. Gerasimov[d] and Andrey A. Rempel[abe]

Received 29th April 2020
Accepted 24th June 2020

DOI: 10.1039/d0ra03862h

rsc.li/rsc-advances

The effect of high-energy milling and long-term annealing on the stability of Ti_2O_3 nanocrystals was studied using a magnetic susceptibility method. *In situ* temperature dependences revealed that the crystal size greatly affects the magnetic susceptibility value. According to XRD, SEM and TEM data, Magnéli phases Ti_9O_{10}, Ti_4O_7, Ti_7O_{19} and Ti_3O_5 are formed.

The titanium–oxygen (Ti–O) system is currently important from both scientific and applied viewpoints.[1] Titanium compounds depending on nonstoichiometry[2–5] are a promising functional material for a wide range of applications, such as a capacitors, photocatalysts for the degradation of organic pollutants in air and water, promising functional materials for renewable energy sources (*e.g.*, solar batteries, photochemical water decomposition and hydrogen generation devices), efficient photoelectric converters, memristor memory elements, *etc.*[6–12] Titanium oxide Ti_2O_3 with unusual properties has a narrow homogeneity region from $TiO_{1.49}$ to $TiO_{1.51}$.[13] There is a d-metal–semiconductor electronic phase transition at 420–550 K without any change in the symmetry and crystal structure. The strong deformation of the crystal lattice with increasing temperature caused the band gap closure.[14–16] Also, Ti_2O_3 exhibits thermoelectrical properties,[17] and doped Ti_2O_3 films have high negative magnetoresistance.[18]

The aim of this work is to study the effect of mechanical treatment (high-energy milling) and subsequent high-temperature annealing in a vacuum on the crystal structure and thermal stability of Ti_2O_3 nanocrystals in the temperature range from 300 to 1200 K with the use of a magnetic susceptibility method.

The initial titanium(III) oxide Ti_2O_3 microcrystals with corundum structure (sp. gr. $R\bar{3}c$) with an average size of about 25 μm were synthesized by solid phase sintering from a mixture of Ti and TiO_2 powders in a vacuum of 10^{-3} Pa at 1770 K. Titanium(III) oxide Ti_2O_3 nanocrystals have been obtained by high-energy milling of Ti_2O_3 microcrystals in a Retsch PM 200 planetary ball mill. The mass ratio of grinding balls made of zirconium dioxide (ZrO_2) stabilized with yttrium oxide (Y_2O_3) to Ti_2O_3 powder in the experiment was 10 : 1. Isopropyl alcohol was used as a grinding liquid. The following milling regime was employed to produce nanopowders: the duration of milling was 15, 30, 60, 120, 240 and 480 min, reversal of rotation direction was each 15 min, the interval between rotation direction reversal was 5 s, the rotation velocity of milling pot backing plate was 500 rpm.

X-ray phase analysis of all powders was performed in $CuK\alpha_{1,2}$-radiation on a Shimadzu XRD-7000 diffractometer in Bragg–Brentano geometry in stepwise scanning mode with $\Delta(2\theta) = 0.02°$ in 2θ angle interval from 10 to 120°. To identify phases, the powder diffraction database ICDD, USA, Release 2016 was used. The phases were analyzed with the use of the Powder Cell 2.4 program. For a full-profile description of X-ray diffraction reflections, the pseudo-Voigt function was used. The diameter of nanocrystals D was determined from diffraction reflection broadening with the Williamson–Hall method.[19,20] The CSR size was obtained by extrapolating the dependence $\beta^*(s)$ to the value $s = 0$, and the magnitude of microstrain was determined from the slope of this dependence.[21,22]

The microstructure of nanocrystals was studied with the high-resolution scanning electron microscopy (SEM) on a ZEISS Ultra 55 microscope. The working distance (WD) was 3.9–4.3 mm, the electron high tension (EHT) was 3–5 keV, and the beam width ranged from 2 to 6 μm depending on magnification. In order to avoid excessive electrization of powder during electron microscope imaging, the examined powder was deposited on a conducting adhesive tape and then was covered with a chromium layer of about 2 to 4 nm thick; the chromium coating did not affect the quality of visualization of powder morphology.

The structure of titanium oxide nanocrystals was determined by using the high-resolution transmission electron microscopy

[a]*Institute of Solid State Chemistry of the Ural Branch of the Russian Academy of Sciences, 620990 Ekaterinburg, Russia. E-mail: anibla_v@mail.ru*

[b]*Ural Federal University, 620002 Ekaterinburg, Russia*

[c]*Institute for Electron Microscopy and Nanoanalysis, Graz University of Technology, A-8010 Graz, Austria*

[d]*Boreskov Institute of Catalysis SB RAS, 630090 Novosibirsk, Russia*

[e]*Institute of Metallurgy of the Ural Branch of the Russian Academy of Sciences, 620016 Ekaterinburg, Russia*

(HRTEM) on a JEM 2010 electron microscope (JEOL, Japan) with accelerating voltage of 200 kV and ultimate lattice resolution of 140 pm. Imaging was performed by means of CCD matrix of Soft Imaging System (Germany). The device was equipped with a Phoenix (EDAX, USA) energy-dispersive characteristic X-ray radiation (EDX) spectrometer with a semiconducting Si(Li)-detector with energy resolution of 130 eV. Ti_2O_3 particles were placed into alcohol and were further deposited on perforated carbon substrates (diameter of holes of about 1 μm) fixed on copper grids. Particles were deposited with the use of a UZD-1UCh2 ultrasonic disperser, which allowed uniform particle distribution on the substrate surface. After the grids were extracted from alcohol, the alcohol evaporated.

Thermal stability and phase transformations with long-term exposure for complete running of processes in the system and structure stabilization were studied with the analysis of magnetic susceptibility variation by using the Faraday method on a pendulum magnetic Domenikalli-type balance in vacuum of about 10^{-3} Pa.[23] Magnetic susceptibility χ of Ti_2O_3 was measured in the temperature interval from 300 to 1200 K in magnetic fields with intensity from 7.2 to 8.8 kOe. The heating and cooling rate of the samples during susceptibility measurements was about 1 K min^{-1}. The powder mass and the crystal structure of Ti_2O_3 were controlled before and after χ measurements. The accuracy of χ measurements was about $\pm 0.05 \times 10^{-6}$ emu g^{-1}. The absence of ferromagnetic impurities in the powders was confirmed by measurements at different magnetic field values.

Detailed analysis of X-ray diffraction patterns of ball milled Ti_2O_3 (Fig. 1a) showed that the crystal structure of nanopowder coincides with the crystal structure of microcrystal (Fig. 1a), *i.e.* the structure of Ti_2O_3 is highly stable with respect to high-energy milling, and fragmentation does not lead to changing of crystal symmetry. After high-energy milling, broadening of reflections is observed on the X-ray diffraction patterns, which is related to a small grain size and the presence of microstrains in the system due to high-energy milling. The full-profile analysis of X-ray diffraction reflections showed a decrease in coherent scattering region (CSR) from 25 μm to 10 nm with an increase of milling time from 15 to 480 minutes, while the microstrain increase up to 0.26%.

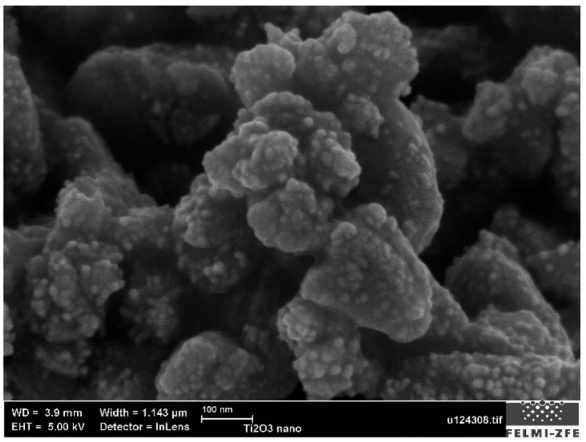

Fig. 2 SEM image of ball milled Ti_2O_3. Small granules of about 10 to 30 nm in size adhere to each other and form agglomerates.

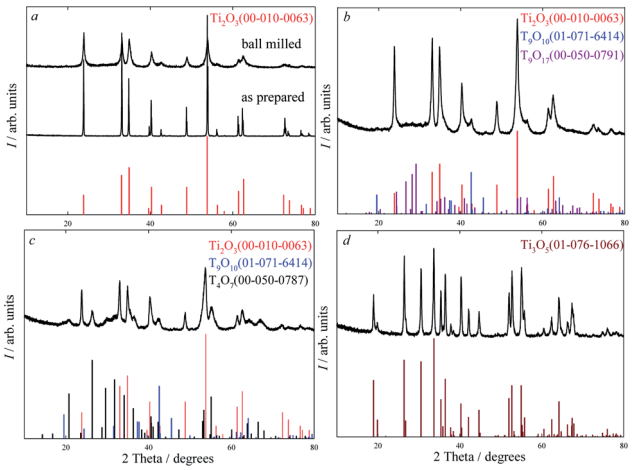

Fig. 1 XRD pattern of powders at room temperature: (a) as prepared microcrystals and ball milled nanocrystals; after magnetic susceptibility measurements: (b) at 673 K; (c) at 873 K; (d) at 1200 K.

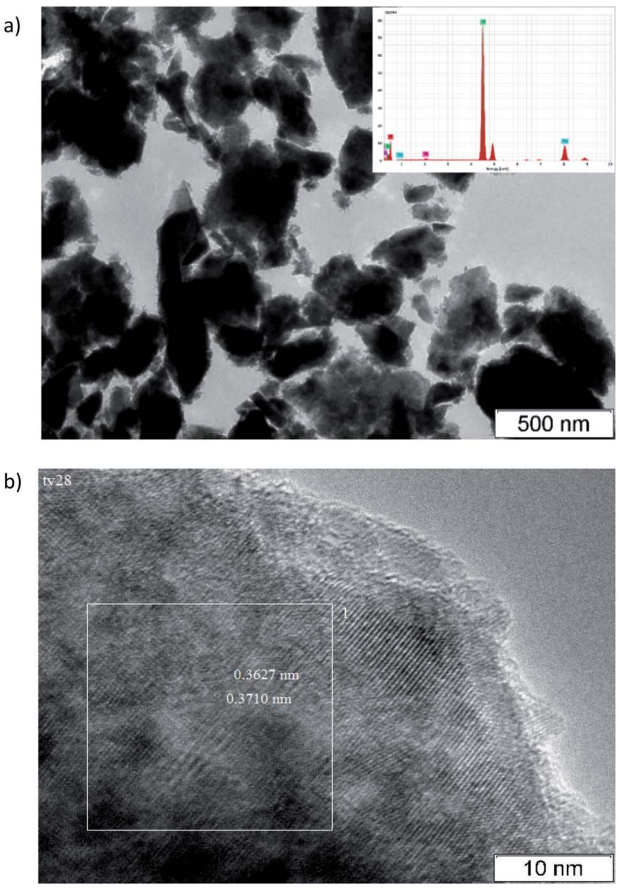

Fig. 3 HRTEM images of Ti_2O_3 nanocrystals: (a) the sample consists mainly of crystallites of sizes from 50 to 500 nm; (b) morphology of milled nanocrystalline Ti_2O_3, the measured d_{hkl} correspond to the Ti_2O_3 phase (PDF 00-010-0063).

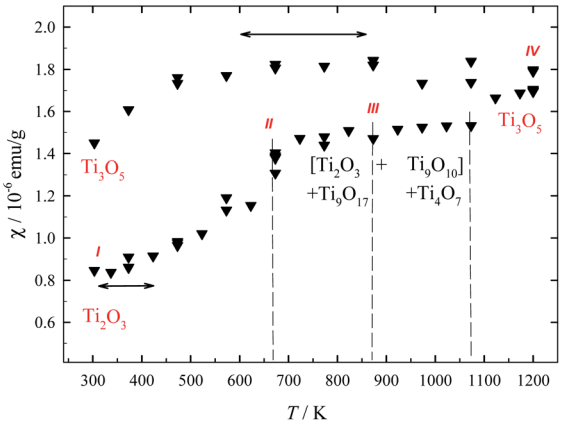

Fig. 4 *In situ* temperature dependences of magnetic susceptibility for Ti_2O_3 nanocrystals. The left-right arrow indicates the reverse behavior of magnetic susceptibility. The figures denote the magnetic susceptibility values at room temperature in different states: I – initial state; after magnetic susceptibility measurements: II – at 673 K, III – at 873 K, IV – at 1200 K.

Analysis of SEM micrographs of ball milled Ti_2O_3 nanocrystals revealed that the particles are uniformly distributed in the bulk and have a granular or rounded shape (Fig. 2). It was found that small granules of about 10–30 nm in size adhere to each other and form agglomerates. Fig. 3 displays a HRTEM image of the ball milled Ti_2O_3 nanocrystal. According to HRTEM data, the sample consists mainly of crystallites of sizes from 50 to 500 nm (Fig. 3a).

According to the observed d_{hkl} (Fig. 3b), this phase corresponds to Ti_2O_3 (PDF 00-010-0063). Thus, the size of particles found with SEM and HRTEM methods coincide, which indicates that the size of CSR of particles determined from XRD data is accurate enough.

The experimental data obtained earlier show that the magnetic susceptibility value of nanocrystals is twice as small in absolute magnitude as that of microcrystals.[24] The crystal size affects greatly not only the value of magnetic susceptibility, but also the temperature behaviour of magnetic susceptibility. The temperature dependence of magnetic susceptibility for Ti_2O_3 microcrystals has a classical form of s-shaped curve typical of first-order phase transitions without considerable hysteresis. Fig. 4 shows *in situ* temperature dependences of magnetic susceptibility for Ti_2O_3 nanocrystals. In the temperature region from 300 to 400 K, the structure of initial Ti_2O_3 nanocrystal remains trigonal (sp. gr. $R\bar{3}c$); the temperature dependence exhibits a reverse behavior of magnetic susceptibility, which shows that the state of nanocrystals in this temperature region is metastable. Annealing of Ti_2O_3 nanocrystals at temperature above 400 K leads to phase transformations and, as a result, to magnetic susceptibility enhancement. X-ray diffraction analysis shows that after annealing to 673 K the powder contains additional phases of Ti_9O_{10} (sp. gr. *Immm*) – 3 mass% and Ti_9O_{17} (sp. gr. $I\bar{1}$) – 11 mass% alongside with Ti_2O_3 phase (sp. gr. $R\bar{3}c$) in the amount of 86 mass% (Fig. 1b). Further annealing and increasing annealing temperature to 873 K result in variation of phases and phase proportions. X-ray diffraction analysis (Fig. 1c) also shows that the powder contains Ti_2O_3 (sp. gr. $R\bar{3}c$) – 38 mass%, Ti_9O_{10} (sp. gr. *Immm*) – 2 mass%, Ti_4O_7 (sp. gr. $A\bar{1}$) – 60 mass%.

It is noteworthy that the Ti_9O_{10} phase (sp. gr. *Immm*), which was first obtained during annealing of nonstoichiometric TiO_y nanocrystal and annealing of TiO_y/HAP nanocomposite,[25–27] is formed during annealing of only titanium oxide nanocrystals with superstoichiometric composition. According to quantum chemical calculations, the Ti_9O_{10} phase (sp. gr. *Immm*) in a microcrystalline state is unfavorable in comparison with the disordered cubic phase of the same $TiO_{9/10}$ composition, therefore its formation is due to size effects.[28,29]

When the annealing temperature rises, the stable Ti_3O_5 with monoclinic structure (sp. gr. *I*2/*c*) is formed (Fig. 1d). Judging by the temperature dependence of magnetic susceptibility (Fig. 4), the formation of the Ti_3O_5 phase occurs at about 1073 K. At further heating from 300 to 1200 K and cooling from 1200 to 300 K, a reverse behavior of magnetic susceptibility is observed, which indicates that the system reaches the equilibrium state. Thus, the experimental results show that the phase stability and

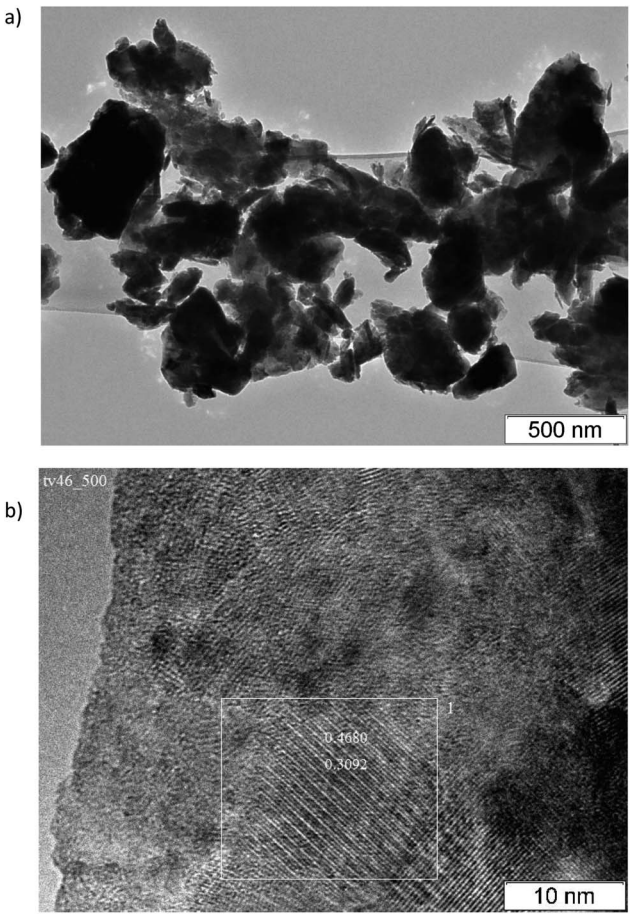

Fig. 5 HRTEM images of Ti_3O_5 nanocrystals: (a) the sample consists of plate-like particles 10 nm to 1 μm in size; (b) well crystallized structure, dimensions of blocks 100 nm, the observed interplanar spacings d_{hkl} correspond to Ti_3O_5 phase (PDF 01-076-1066).

phase transitions in Ti_2O_3 are greatly affected above all by the crystal sizes.

Fig. 5 demonstrates the HRTEM micrographs of nanocrystalline powder after annealing experiments. The sample consists of plate-like particles 10 nm to 1 μm in size (Fig. 5a). Regions with well crystallized structure are observed where the dimensions of blocks are 100 nm. According to the observed interplanar spacings, the phase formed corresponds to the Ti_3O_5 phase (Fig. 5b) with monoclinic structure (sp. gr. *I*2/c) (PDF 01-076-1066).

Thus, Ti_2O_3, subjected to mechanical treatment (high-energy milling) and heat treatment in the temperature range from 300 to 1200 K in vacuum, is an unstable phase since it changes during thermal treatment. According to the X-ray diffraction analysis, SEM and HRTEM data, the Ti_9O_{10} phase and Magnelli phases Ti_4O_7, Ti_7O_{19} and Ti_3O_5 are formed depending on the annealing temperature. In addition, the *in situ* temperature dependences of magnetic susceptibility showed that the crystal size greatly affects the value of magnetic susceptibility; the magnetic susceptibility value of nanocrystals is twice as small in absolute magnitude as that of microcrystals.

Conflicts of interest

There are no conflicts to declare.

Acknowledgements

The reported study was funded by RFBR according to the research project no. 19-03-00051a.

References

1 X. Chen and S. S. Mao, *Chem. Rev.*, 2007, **107**, 2891.
2 A. A. Valeeva, S. Z. Nazarova and A. A. Rempel, *Phys. Solid State*, 2016, **58**(4), 771.
3 A. A. Valeeva and A. A. Rempel, *Mendeleev Commun.*, 2010, **20**, 101.
4 A. A. Valeeva, A. A. Rempel and A. I. Gusev, *Dokl. Phys.*, 2002, **47**, 39.
5 M. G. Kostenko, A. A. Valeeva and A. A. Rempel, *Mendeleev Commun.*, 2012, **22**, 245.
6 V. Schöllmann, J. Johansson, K. Andersen and D. V. Haviland, *J. Appl. Phys.*, 2000, **88**, 6549.
7 A. A. Rempel, E. A. Kozlova, T. I. Gorbunova, S. V. Cherepanova, E. Y. Gerasimov, N. S. Kozhevnikova, A. A. Valeeva, E. Y. Korovin, V. V. Kaichev and Y. A. Shchipunov, *Catal. Commun.*, 2015, **68**, 61.
8 A. A. Valeeva, E. A. Kozlova, A. S. Vokhmintsev, R. V. Kamalov, I. B. Dorosheva, A. A. Saraev, I. A. Weinstein and A. A. Rempel, *Sci. Rep.*, 2018, **8**, 9607.
9 A. A. Valeeva, I. B. Dorosheva, E. A. Kozlova, R. V. Kamalov, A. S. Vokhmintsev, D. S. Selishchev, A. A. Saraev, E. Y. Gerasimov, I. A. Weinstein and A. A. Rempel, *J. Alloys Compd.*, 2019, **796**, 293.
10 D. Recatalá, R. Llusar, A. L. Gushchin, E. A. Kozlova, Y. A. Laricheva, P. A. Abramov, M. N. Sokolov, R. Gómez and T. Lana-Villarreal, *ChemSusChem*, 2015, **8**, 148.
11 N. S. Kolobov, D. A. Svintsitskiy, E. A. Kozlova, D. S. Selishchev and D. V. Kozlov, *Eng. J.*, 2017, **314**, 600.
12 A. S. Vokhmintsev, I. A. Weinstein, R. V. Kamalov and I. B. Dorosheva, *Bull. Russ. Acad. Sci.: Phys.*, 2014, **78**, 932.
13 S. Andersson, B. Collén, U. Kuylenstierna and A. Magnéli, *Acta Chem. Scand.*, 1957, **11**, 1641.
14 H. Fan, M. Wang, Z. Yang, X. Ren, M. Yin and S. Liu, *Appl. Phys. A: Mater. Sci. Process.*, 2016, **122**, 964.
15 J. Wang, Y. Li, L. Deng, N. Wei, Y. Weng, S. Dong, D. Qi, J. Qiu, X. Chen and T. Wu, *Adv. Mater.*, 2016, **29**, 1603730.
16 A. I. Poteryaev, A. I. Lichtenstein and G. Kotliar, *Phys. Rev. Lett.*, 2004, **93**, 086401.
17 I. Veremchuk, I. Antonyshyn, C. Candolfi, X. Feng, U. Burkhardt, M. Baitinger, J. T. Zhao and Y. Grin, *Inorg. Chem.*, 2013, **52**, 4458.
18 Z. Wang, Y. Hong, J. Tang, C. Radu, Y. Chen, L. Spinu, W. Zhou and L. D. Tung, *Appl. Phys. Lett.*, 2004, **86**, 7384.
19 W. H. Hall, *Proc. Phys. Soc., London, Sect. A*, 1949, **62**, 741.
20 G. K. Williamson and W. H. Hall, *Acta Metall.*, 1953, **1**, 22.
21 A. A. Valeeva, H. Schroettner and A. A. Rempel, *Russ. Chem. Bull.*, 2014, **63**, 2729.
22 A. A. Valeeva, S. Z. Nazarova and A. A. Rempel, *Phys. Status Solidi B*, 2016, **253**, 392.
23 A. A. Valeeva, S. Z. Nazarova and A. A. Rempel, *JETP Lett.*, 2015, **101**, 258.
24 A. A. Valeeva, S. Z. Nazarova and A. A. Rempel, *J. Alloys Compd.*, 2020, **817**, 153215.
25 S. V. Rempel, A. A. Valeeva, E. A. Bogdanova, H. Schroettner, N. A. Sabirzyanov and A. A. Rempel, *Mendeleev Commun.*, 2016, **26**, 543.
26 S. V. Rempel, D. A. Eselevich, E. Y. Gerasimov and A. A. Valeeva, *J. Alloys Compd.*, 2019, **800**, 412.
27 S. V. Rempel, E. A. Bogdanova, A. A. Valeeva, H. Schroettner, N. A. Sabirzyanov and A. A. Rempel, *Inorg. Mater.*, 2016, **52**, 476.
28 A. A. Valeeva, M. G. Kostenko, S. Z. Nazarova, E. Y. Gerasimov and A. A. Rempel, *Inorg. Mater.*, 2018, **54**, 568.
29 M. G. Kostenko and A. A. Valeeva, *Mendeleev Commun.*, 2019, **29**, 405.

